Optically-Interrogated Zero-Power MEMS Magnetometer

Daniel J. Vasquez, *Student Member, IEEE*, and Jack W. Judy, *Senior Member, IEEE*

Abstract—A magnetic-field-sensing system that consists of a miniature zero-power magnetometer, an integrated micromachined corner-cube reflector (CCR), a commercially available diode laser, and a photodetector array, has been designed, fabricated, assembled, and tested. The zero-power-magnetometer design is based on a ferromagnetic MEMS magnetometer, which consists of a permanent magnet that is torsionally suspended to allow rotation about a single axis. A single mirror of the CCR is attached to the magnetometer torsion beam. When the magnet rotates in response to a change in magnetic field, the torsion beam will twist and cause the mirror to become misaligned. The non-ideality of the CCR can be interrogated with a laser and a photosensor array can be used to measure the reflected signal. This method of magnetic sensing completely eliminates sensor-node power consumed at the remote location. The sensor node developed for this paper occupies a volume of only 1.5 mm^3 and can detect a magnetic field between 820 A/m to 6 kA/m with an uncertainty of 90 A/m at a 1-m optical-interrogation range. The primary application of this technology is in wireless sensing systems that must operate continuously without providing or maintaining the sensor-node energy (e.g., replacing batteries or scavenging energy) or in extremely harsh environments where power supplies and integrated circuits (IC) are not an option.　　　　**[1616]**

Index Terms—Ferromagnetic materials, magnets, magnetometers, microelectromechanical devices, microsensors, multisensor systems, optical device fabrication, optical diffraction.

I. INTRODUCTION

ADVANCES in hardware design and energy-efficient network protocols make it possible to design networks consisting of hundreds or thousands of sensor nodes. These networks can enable the constant monitoring of our environment while also providing a means for scientists and researchers to query geographic locations of interest. Applications for such networks range from groundwater contaminant sensors [1] to smart buildings and factories [2] and ferrous-material detection (e.g., tanks, jeeps, and weapons) [3]–[6]. A sensor node typically consists of five components: sensing hardware, processor, memory, power supply, and transceiver [2], [8]. Prof. Pister's group at U.C. Berkeley has been working to build a single sensor node containing all of the above components in a cubic millimeter and have published results on a 16-mm^3 node [9].

Because battery technology has not kept pace with hardware advances, the power supply of sensor networks, along with single-node cost, has become the bottleneck in designing sensor networks with the scale and density needed for many applications. The limitations caused by batteries have led to research in alternative power supplies to enable self-sustaining sensor nodes that can generate their own power through remote and self-powering techniques. As mentioned above, cost can also be a prohibitive factor in sensor-network deployment. To make dense sensor networks feasible, it is necessary for a single node to be made as cheaply as possible.

Along with power and cost limitations, durability is another concern for deploying sensor nodes in harsh or hostile locations. Applications with the harshest environmental demands include those in the industrial, automotive, and aerospace domains, where nodes can be subjected to temperatures from 200 to 600 °C [10]. Temperatures in this range can eliminate the possibility of using conventional batteries and ICs on sensor nodes since each technology exhibits a severe performance degradation when subjected to temperatures greater than 150 °C [10]. By eliminating the need for batteries, circuitry, and an onboard radio, our zero-power corner-cube reflector (CCR) sensors can potentially be designed to withstand high-temperature environments up to the Curie temperature of the magnetic material, be produced cheaply, and occupy a small volume [7]. The major requirement for zero-power CCR sensor nodes is that they remain within line of sight of a base station.

II. FERROMAGNETIC MEMS MAGNETOMETERS

In this section, a microelectromechanical systems (MEMS)-based ferromagnetic magnetometer will be discussed. The operation of a ferromagnetic MEMS magnetometer is similar to a microcompass, where magnetic field intensity is translated into mechanical movement [3]–[7]. The presence of a magnetic field produces a torque on the magnetic element, which causes it to rotate along the axis of the supporting torsion beam. However, the rotation of the magnet is opposed by the mechanical restoring torque of the torsion beam. Consequently, the magnet will rotate until the mechanical and magnetic torques are equal [Fig. 1].

In a magnetic field $\vec{H}$, the torque experienced by the permanent magnet is expressed as

$$\vec{T}_{\text{mag}} = (\mu_0 \vec{M} \times \vec{H}) V_{\text{mag}} \qquad (1)$$

with magnetization $\vec{M}$ and volume V_{mag} of the ferromagnetic material. However, the magnet is attached to the substrate
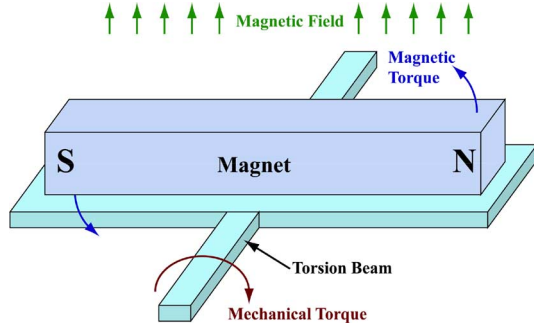
Fig. 1. Diagram of a ferromagnetic MEMS magnetometer that illustrates the induced magnetic and mechanical torques.

through two torsion beams that will counter the rotation generated by the torque due to the applied magnetic field. The mechanical counter torque generated by the torsion beams is equal to

$$\vec{T}_{\text{mech}} = k_\phi \vec{\phi}_{\text{mag}} \qquad (2)$$

with rotational spring constant k_ϕ and rotational deflection of the permanent magnet $\vec{\phi}_{\text{mag}}$. In equilibrium, the two torques will balance ($\vec{T}_{\text{mag}} = \vec{T}_{\text{mech}}$) and a stable angle of deflection will be achieved. By equating (1) and (2) and solving for $\vec{\phi}_{\text{mag}}$, the resulting angular deflection of a ferromagnetic MEMS magnetometer is found to be

$$\vec{\phi}_{\text{mag}} = \frac{(\mu_0 \vec{M} \times \vec{H}) V_{mag}}{k_\phi}. \qquad (3)$$

A. Scaling Properties

For widely distributed sensor systems, smaller sensors are generally preferred due to a corresponding reduction in power and an improvement in deployability and covertness. Because size is important, it is necessary to consider how the sensitivity of the device scales. The torque experienced by the magnet as shown by (1) is proportional to the magnetic volume and thus has a cubic dependence on the scale of the linear dimension. However, the opposing mechanical torque also scales cubically and can be expressed as

$$\vec{T}_{\text{mech}} = \frac{KG}{L} \phi_{\text{mag}}$$
$$\approx ab^3 \left[\frac{16}{3} - 3.36 \frac{b}{a} \left(1 - \frac{b^4}{12a^4} \right) \right] \frac{G}{L} \vec{\phi}_{\text{mag}} \propto s^3 \quad (4)$$

with half the beam width a, half the beam thickness b, beam length L, and shear modulus G. K is a shape-dependent factor that scales as s^4. Since the torsional spring constant is proportional to the ratio of shape factor over the length of the torsion beam, the total mechanical torque scales cubically with linear dimension. Since both the magnetic torque and the mechanical torque scale cubically with linear dimension, the responsivity, which is proportional to the ratio of magnetic torque over the mechanical torque, does not scale with dimension. Consequentially it is possible to greatly miniaturize magnetometers of this design.
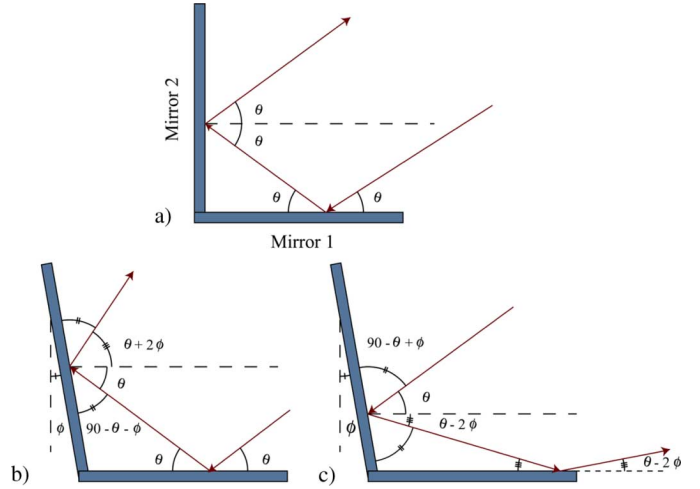

Fig. 2. Ray-tracing example of (a) an ideal 2-D CR and a nonideal 2-D CR entering from both (b) Mirror 1 and (c) Mirror 2. In this example, it is illustrated that the reflected directions from examples (b) and (c) will always have a full angle of 4ϕ between them regardless of incident direction.

III. CORNER-CUBE REFLECTOR

Radio transmitters in wireless nodes typically consume the largest fraction of the overall sensor-node power. Present wireless components using IEEE 802.11 wireless cards can consume up to 1.6 W while in the transmit state, and the power consumption only drops to 1.4 W in the receive state [11], [12]. Even though smaller and lower power wireless systems exist for sensor networks, such as the Mica2Dot from Xbow, they still use a radio with substantial power consumption (i.e., 80 mW in transmit and 24 mW in receive).[1]

Passive optical transmitters using mirrors to reflect an interrogating laser have been used to eliminate the power consumed by the sensor-node radio [9], [13], [14]. These optical systems use digitally modulated CCRs to either reflect an interrogating laser back towards the source or scatter the laser away from the source. A CCR is a simple device consisting of three mirrors. In the ideal case, each mirror is completely orthogonal to the other two mirrors. Light that reflects off of all three mirrors will be reflected directly back towards the source regardless of the incident direction. In the case of digital optical-CCR transmitters, two of the mirrors are fixed and orthogonal to each other, while the third mirror can be electrostatically actuated to change its angular orientation. When the third mirror is actuated to be nonorthogonal to the two other mirrors, the light will be scattered away from the incident direction of the source. However, when the electrostatic actuator positions the third mirror to become mutually orthogonal to the other two mirrors, incident light is reflected directly back towards the source.

The digital optical-CCR technology is useful for wireless sensor systems that use a smaller number of sophisticated base stations to interrogate a larger number of low-power sensor nodes. Although in such systems power is distributed to the base stations using conventional means, the actual sensor node power consumption has been significantly reduced. The power savings is due to the fact that each node now only

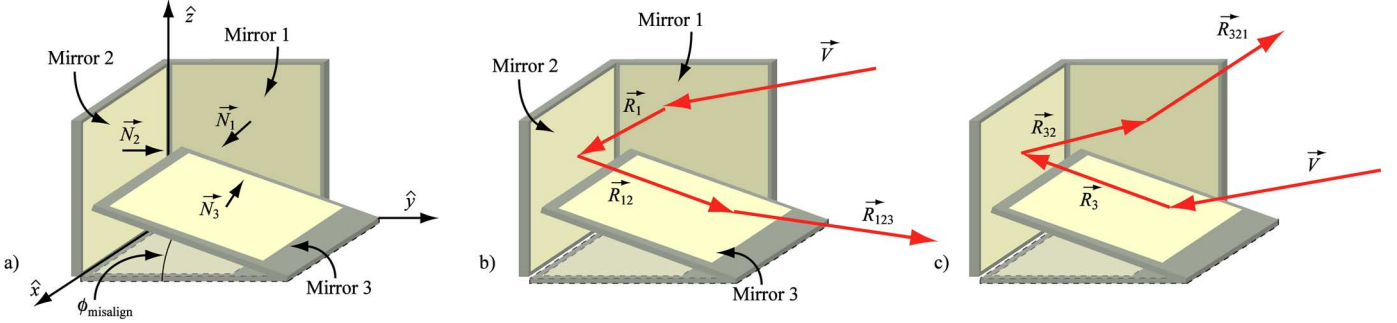[1]Crossbow Technology, San Jose, CA, www.xbow.com.

Fig. 3. (a) Coordinate system and ray-tracing example for a CCR that illustrates the vector naming convention for reflected optical paths through a CCR with reflected (b) directions R_{123} and (c) R_{321}. The subscripts keep track of the path through the CCR with the optical beam in example (b) taking the path from Mirror 1 to Mirror 2 and exiting after striking Mirror 3. The path in example (c) is from Mirror 3 to Mirror 2 and exits after striking Mirror 1.

requires power for the sensor and the integrated circuitry, not a power-intensive radio.

A. Ray Tracing Through a CCR

To understand how a CCR can be extended for use in analog-data transmission, one first needs to understand what effect misaligning a single mirror in a CCR will have on the reflected optical beam. As the first step to studying mirror misalignment in a corner cube, all paths through the CCR must be ray-traced assuming a single mirror misalignment of ϕ_{misalign}. The mirror names, coordinate system, and normals are defined in Fig. 3(a). As a convention, Mirror 1 is a static mirror with normal $\vec{N}_1$ in the $\langle 100 \rangle$ direction, Mirror 2 is a static mirror with normal $\vec{N}_2$ in the $\langle 010 \rangle$ direction, and Mirror 3 is the modulated mirror with normal $\vec{N}_3$ in the $\langle 0, \sin(\phi_{\mathrm{misalign}}), \cos(\phi_{\mathrm{misalign}}) \rangle$ direction Fig. 3(a).

For light reflecting off a single mirror with unit normal $\vec{N}$ and unit incident direction $\vec{V}$, the reflected direction $\vec{R}$ of unit magnitude is given by

$$\vec{R} = \vec{V} - 2\vec{N}(\vec{V} \bullet \vec{N}). \qquad (5)$$

To find the reflected direction of a path through the CCR, (5) is repeated for each of the three mirrors in the path. However, it should be noted that there are six unique paths that light can take through a CCR, and each path can result in a unique reflected direction. To illustrate the multiple distinct reflected optical beams, a two-dimensional corner reflector (CR) with a single mirror misalignment of ϕ is first examined (Fig. 2). Light can enter the corner by striking Mirror 1 then exit after striking Mirror 2 [Fig. 2(b)] or by striking Mirror 2 first then exit after striking Mirror 1 [Fig. 2(c)]. As seen from Fig. 2, the reflected directions of the two different paths have an angle between them of 4ϕ, regardless of incident direction.

While ray tracing through a three-dimensional (3-D) CCR, the convention illustrated in Fig. 3 is used to keep track of the optical-beam path through the CCR. As seen from Fig. 3(b), $\vec{R}_1$ is the reflected direction of an optical beam with incident direction $\vec{V} = \langle -V_x, -V_y, -V_z \rangle$ reflecting off of Mirror 1 and is evaluated as

$$\vec{R}_1 = \vec{V} - 2\vec{N}_1(\vec{V} \bullet \vec{N}_1)$$
$$= \langle V_x, -V_y, -V_z \rangle. \qquad (6)$$

The reflected direction $\vec{R}_{12}$ of $\vec{R}_1$ reflecting off of Mirror 2 is

$$\vec{R}_{12} = \vec{R}_1 - 2\vec{N}_2(\vec{R}_1 \bullet \vec{N}_2)$$
$$= \langle V_x, V_y, -V_z \rangle. \qquad (7)$$

The reflected direction $\vec{R}_{123}$ of $\vec{R}_{12}$ reflecting off of Mirror 3 is the resulting direction of an optical beam in a CCR that reflects off of Mirror 1, Mirror 2, and then Mirror 3. The direction $\vec{R}_{123}$ can be evaluated as

$$\vec{R}_{123} = \vec{R}_{12} - 2\vec{N}_3(\vec{R}_{12} \bullet \vec{N}_3)$$
$$= \langle V_x, V_y \cos(2\phi_{\mathrm{misalign}}) + V_z \sin(2\phi_{\mathrm{misalign}})$$
$$- V_y \sin(2\phi_{\mathrm{misalign}}) + V_z \cos(2\phi_{\mathrm{misalign}}) \rangle. \qquad (8)$$

The reflected direction of an optical beam, which has a path through the CCR that goes from Mirror 3 to Mirror 2 and exits after striking Mirror 1, is $\vec{R}_{321}$ [Fig. 3(c)] and can be determined with a procedure similar to that used to derivate $\vec{R}_{123}$.

By determining the reflected directions for each of the six different optical paths through a CCR, it is observed that, for a 3-D CCR with one misaligned mirror, there are only two unique reflected directions. Namely, the reflected directions $\vec{R}_{123}$, $\vec{R}_{231}$, and $\vec{R}_{213}$ are parallel and $\vec{R}_{321}$, $\vec{R}_{312}$, and $\vec{R}_{132}$ are parallel. It is interesting to note that the order of Mirror 2 and Mirror 3 in the path will determine whether the resultant direction is parallel to $\vec{R}_{123}$ or $\vec{R}_{321}$. The order of Mirror 1 in the path has no effect on determining the output path because Mirror 1 always remains perpendicular to both Mirrors 2 and 3, regardless of the angle of misalignment of Mirror 3. Mirror 1 can be shown to be always perpendicular to both Mirror 2 and Mirror 3 by noting that the dot product of the normals of Mirror 1 and Mirror 2 (9) and Mirror 1 and Mirror 3 (10) are both equal to zero

$$\vec{N}_1 \bullet \vec{N}_2 = \langle 100 \rangle \bullet \langle 010 \rangle = 0 \qquad (9)$$
$$\vec{N}_1 \bullet \vec{N}_3 = \langle 100 \rangle \bullet \langle 0, \sin(\phi_{\mathrm{misalign}}), \cos(\phi_{\mathrm{misalign}}) \rangle$$
$$= 0. \qquad (10)$$

Although in the two-dimensional (2-D) CR the angle between the two reflected beams was always 4ϕ regardless of incident direction, this assumption cannot be made for a 3-D CCR. Because $\vec{R}_{123}$ and $\vec{R}_{321}$ are both unit vectors, the angle between the two optical beams $(\theta_{R_{123}R_{321}})$ can be determined by

$$\cos(\theta_{R_{123}R_{321}}) = (\vec{R}_{123} \bullet \vec{R}_{321}) \qquad (11)$$
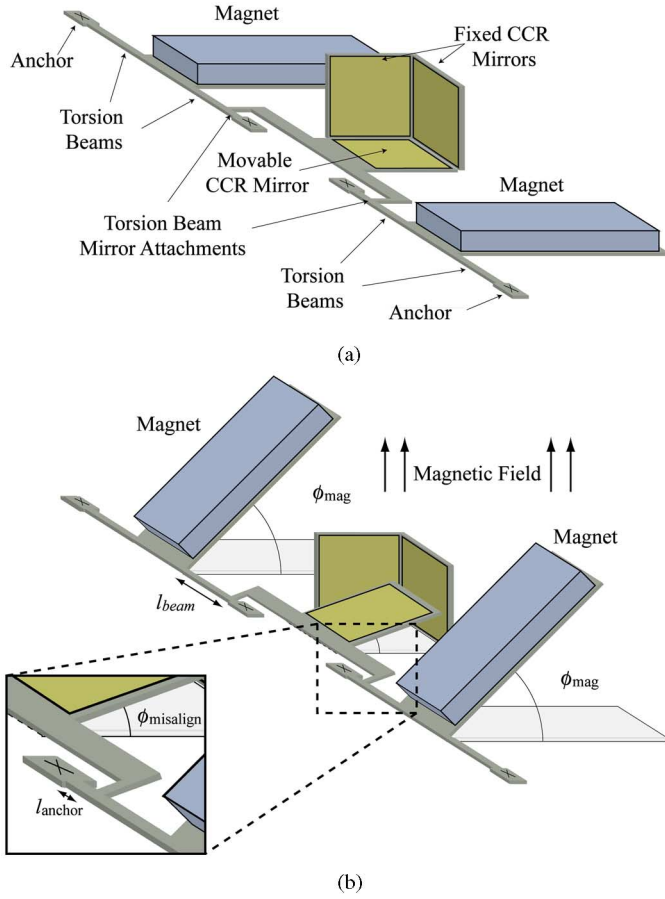
(a)

(b)

Fig. 4. Illustration of zero-power MEMS magnetometer (a) without and (b) with an external magnetic field applied. A closeup view of the coupling between the mirror and torsion beam is also shown.

(a)

(b)

Fig. 5. Scanning electron microscope image of CCR (a) before and (b) after assembly.

given that

$$\vec{R}_{123} \bullet \vec{R}_{321} = V_x^2 + \left(V_y^2 + V_z^2\right)\cos(4\phi_{\mathrm{misalign}}). \quad (12)$$

By using the small-angle approximation, $\theta_{R_{123}R_{321}}$ can be expressed as

$$\theta_{R_{123}R_{321}} \approx 4\phi_{\mathrm{misalign}}\sqrt{V_y^2 + V_z^2}. \quad (13)$$

Equation (13) is consistent with the case where V_x is zero (i.e., incident direction is parallel to Mirror 1), which is equivalent to the two-dimensional case analyzed before. It is seen that indeed the angle between the two unique reflected beams becomes $4\phi_{\mathrm{misalign}}$. This is also the incident direction that results in the maximum angle between the two reflected optical beams for a given angle of misalignment for Mirror 3. In the opposite extreme (i.e., V_y and V_z are both zero), the angle between the two reflected beams is always zero regardless of mirror misalignment. From (13) it can also be seen that the angle between the two reflected optical beams is always some scaling factor between zero and four multiplied by ϕ_{misalign}.

B. Dependence on Incident Direction

From (13), one can see that the angle between the two reflected optical beams is a function of both the mirrors for their signals to be distinguished (e.g., different
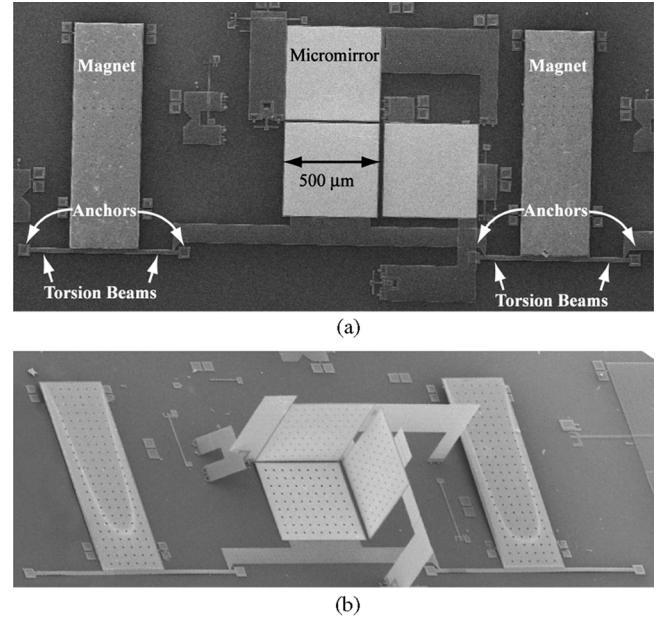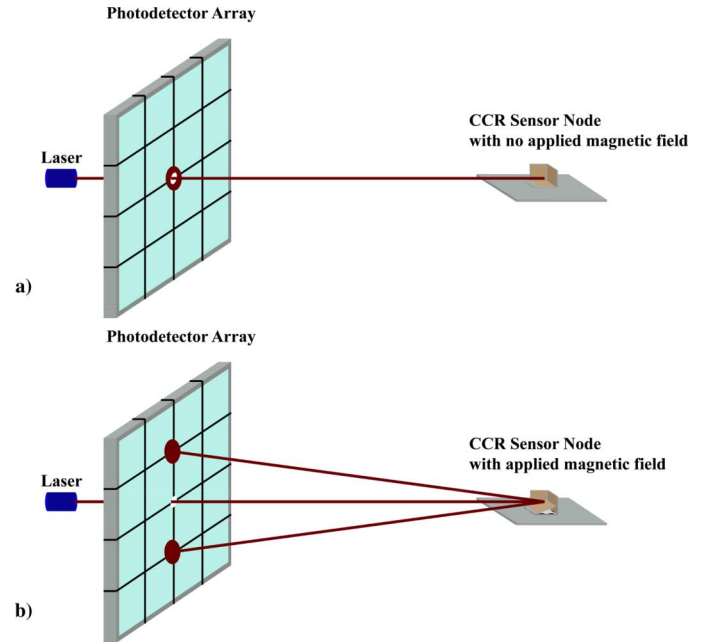

Fig. 6. Illustration of zero-power MEMS magnetometer sensing system (a) without and (b) with an external magnetic field applied.

misalignment and the incident direction of the incoming laser. It is proposed that a CCR can be used for analog data transmission by measuring the angle between the two optical beams reflected from the CCR. The dependence on incident direction is a nonideality in terms of measuring the optical-beam angle if the orientation of the CCR is not known. For applications where the sensor location and orientation can be determined and calibrated prior to data acquisition, the dependence on incident direction is a minor calibration concern. However, applications that do not allow knowledge of the orientation of the CCR are more complicated. For these cases, we propose to integrate a calibration CCR

a) $R = 7.5$ m
$L_{\text{Mirror}} = 38.1$ μm

b) $R = 8.75$ m
$L_{\text{Mirror}} = 44.45$ μm

c) $R = 10$ m
$L_{\text{Mirror}} = 50.8$ μm

d) $R = 11.25$ m
$L_{\text{Mirror}} = 57.15$ μm

$\phi_{\text{misalign}} = 8.3$ mrad $\phi_{\text{misalign}} = 7.1$ mrad $\phi_{\text{misalign}} = 6.2$ mrad $\phi_{\text{misalign}} = 5.6$ mrad

$\phi_{\text{misalign}} = 16.6$ mrad $\phi_{\text{misalign}} = 14.2$ mrad $\phi_{\text{misalign}} = 12.4$ mrad $\phi_{\text{misalign}} = 11.2$ mrad

$\phi_{\text{misalign}} = 24.9$ mrad $\phi_{\text{misalign}} = 21.3$ mrad $\phi_{\text{misalign}} = 18.6$ mrad $\phi_{\text{misalign}} = 16.8$ mrad

$\phi_{\text{misalign}} = 33.2$ mrad $\phi_{\text{misalign}} = 28.4$ mrad $\phi_{\text{misalign}} = 24.8$ mrad $\phi_{\text{misalign}} = 22.4$ mrad
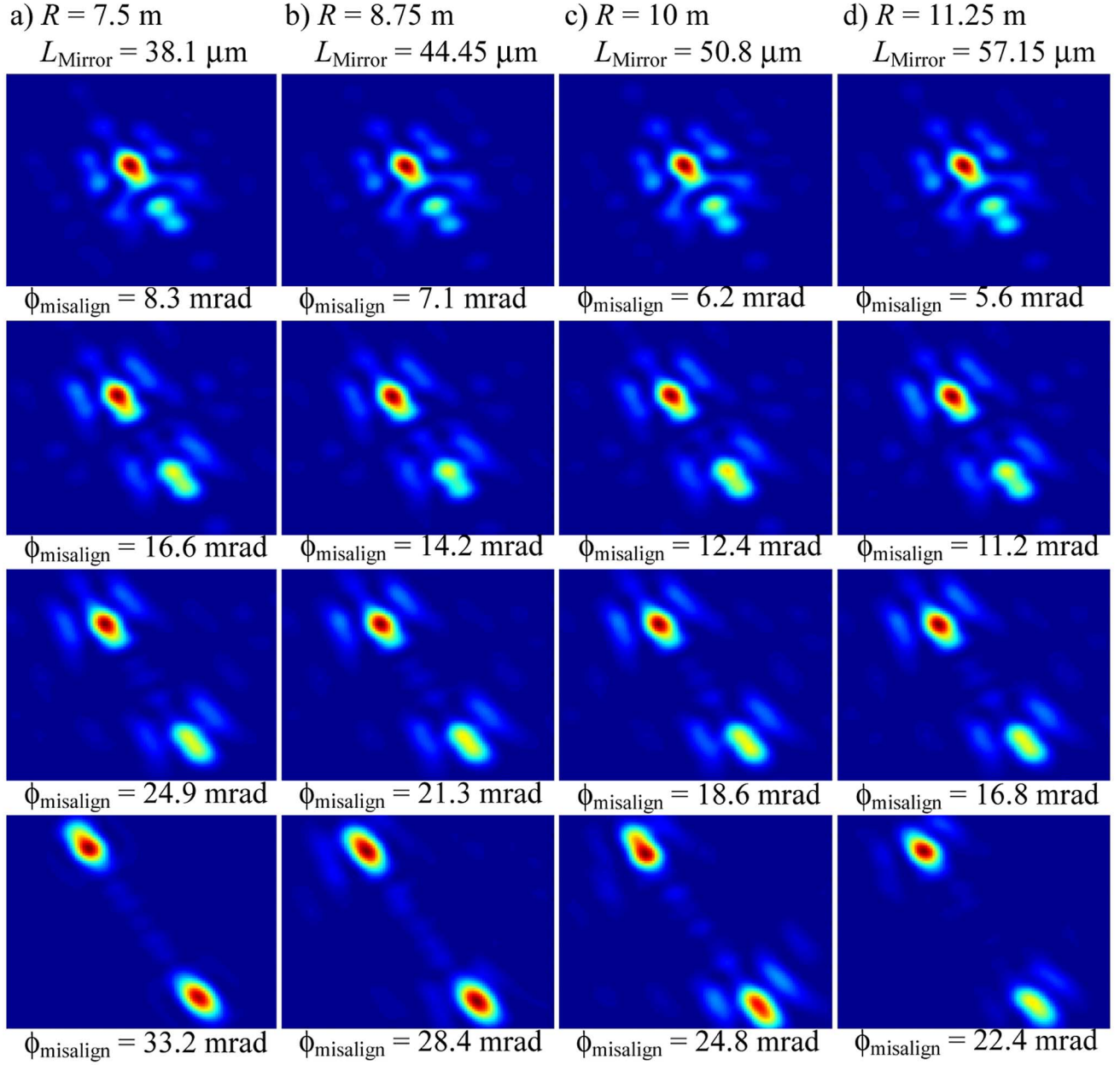
Fig. 7. Simulation results obtained using 3-D wave-optics simulation. Observation and interrogation was measured in the $\langle 111 \rangle$ direction using a simulated 1 m^2 photodetector. In this figure, each column (a, b, c, and d) represents a different CCR mirror size and observation range. Within each column, each CCR technology was simulated over a range of mirror misalignments. This figure illustrates that by scaling the observation range proportional to the mirror size and inversely scaling the mirror misalignment with the mirror size, the resultant image projected onto a fixed size photodetector array will remain the same. (a) $R = 7.5$ m, (b) $R = 8.75$ m, (c) $R = 10$ m, and (d) $R = 11.25$ m.

with a known $\phi_{\text{misalign}-\text{known}}$ next to the analog CCR sensor. Both the calibration and analog CCR sensor need to be packaged in a manner that allow optical filters). Under this scenario, the angle of misalignment of the analog CCR ($\phi_{\text{misalign}-\text{analog}}$) is found to be

$$\phi_{\text{misalign}-\text{analog}} = \frac{\theta_{R_{123}R_{321}-\text{analog}}}{\theta_{R_{123}R_{321}-\text{known}}} \phi_{\text{misalign}-\text{known}}$$

$$\approx \frac{x_{R_{123}R_{321}-\text{analog}}/r_{\text{analog}}}{x_{R_{123}R_{321}-\text{known}}/r_{\text{known}}}$$

$$\times \phi_{\text{misalign}-\text{known}} \qquad (14)$$

with angle between the reflected optical beams from the calibration CCR $\theta_{R_{123}R_{321}-\text{known}}$, angle between the reflected optical beams from the analog CCR $\theta_{R_{123}R_{321}-\text{analog}}$, displacement of the reflected optical beams from the calibration CCR $x_{R_{123}R_{321}-\text{known}}$ at a distance of r_{known} away from the calibration CCR, and displacement of the reflected optical beams from the analog CCR $x_{R_{123}R_{321}-\text{analog}}$ at a distance of r_{analog} away from the analog CCR. Because both the analog and calibration CCRs are fabricated on the same die, r_{known} is equal to r_{analog} and (14) simplifies to

$$\phi_{\text{misalign}-\text{sensor}} = \frac{x_{R_{123}R_{321}-\text{sensor}}}{x_{R_{123}R_{321}-\text{known}}} \phi_{\text{misalign}-\text{known}}. \qquad (15)$$
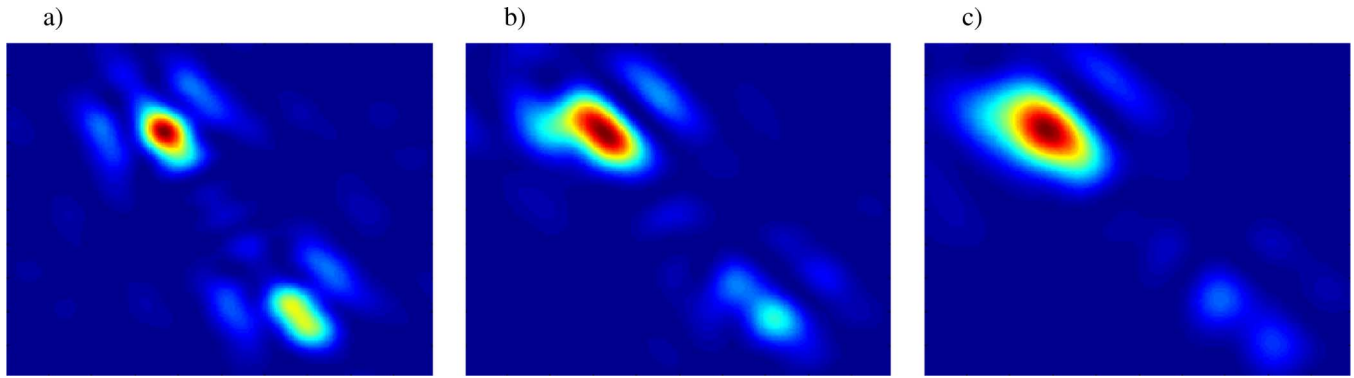
Fig. 8. Simulation results obtained using 3-D wave-optics simulation. Observation and interrogation was measured in the (a) $\langle 111 \rangle$, (b) $\langle 223 \rangle$, and (c) $\langle 112 \rangle$ directions using a simulated 1 m^2 photodetector at a range of 11.25 m. Results are for a CCR with mirrors 57.15 μm wide with a mirror misalignment of 16.8 mrad.

From (15), it can be seen that only the displacement between the optical beams is important and that the observation distance and incident direction fall out of the equation.

IV. ZERO-POWER SENSOR NODE

The work done for the sensor nodes discussed in this paper combines both the ferromagnetic-MEMS magnetometer and CCR technologies. A single sensor node contains two identical ferromagnetic magnetometers and a CCR whose variable mirror is coupled to the rotation of the ferromagnetic magnetometer [Fig. 4]. Because the magnetic elements will rotate to an angle proportional to the magnetic field and a mirror is coupled to the rotation of the magnetic elements, the mirror rotation and consequently the optical displacement is obtained without any power consumption. As shown in Fig. 4, the mirror is not attached directly to the magnetic elements but is instead attached to the torsion beam. Attaching the mirror to the torsion beam increases the simplicity of testing because it allows for control of the mirror in the milliradian range, even though it is difficult to control the magnetic element with less than 10–20° of rotation.

V. FABRICATION

The zero-power magnetometers were fabricated using multiusers MEMS processes (MUMPs) [15],[2] which is a standard surface-micromachining foundry process. The MUMPs process consists of a 2-μm-thick and a 1.5-μm-thick polysilicon structural layer, two sacrificial oxides, and a gold layer. While the MUMPs process provided enough structural layers for the design of the CCRs, it does not contain any ferromagnetic layers. An extra layer of CoNi was electroplated onto the chips in a postprocessing step. The final gold layer of the MUMPs process was used as the seed layer for the electrodeposition. First, a 100-nm-thick Ti layer was deposited across the entire chip using an e-beam evaporator (CHA mark 40). Next, the plating mold is defined using photolithography with Shipley SJR5640 positive photoresist. The exposed Ti conduction layer is then removed over the seed layer in a 1:100 HF solution. Finally, CoNi was electroplated onto the gold seed layer [16], the photoresist was stripped [Fig. 5(a)], the entire structure was released in 49% HF for 4 min, and then the CCRs were carefully assembled [Fig. 5(b)].

[2]MEMSCAP, Bernin, France, www.memscap.com

VI. SYSTEM OVERVIEW

The entire system consists of a miniature zero-power magnetometer, an integrated micromachined CCR, a commercially available diode laser, and a photodetector array [Fig. 6]. The remote sensor node consists of the miniature zero-power magnetometer and CCR. The local base station consists of the commercially available diode laser and the photodetector array.

The diode laser is used to interrogate the CCR on the remote magnetometer. When the sensed magnetic field is zero, all three mirrors on the CCR are perpendicular to one another and the reflected optical beam will travel directly back toward the source. However, a single mirror on the CCR will rotate to an angle proportional to the magnetic field and will cause the reflected optical beam to be split into two beams. The photodetector array is used to measure the displacement between the optical beams. If the orientation of the CCR and the distance between the CCR and the photodetector array are known, then the angle between the optical beams and total remote magnetic field can be determined. For applications where the incident direction and distance is not known, a calibration CCR needs to be incorporated onto the sensor node.

VII. OPERATIONAL RANGE OF CCR SENSORS

To determine the operational range of a CCR sensor node, a simple wave-optics simulation was developed to calculate the interference patterns from the reflected optical signal at various distances. For the wave-optics solution to avoid aliasing, each mirror in the simulation must be broken into elements smaller than half the wavelength of the interrogating laser. Because each mirror is 500 μm wide, the runtime quickly becomes too excessive to perform on a single PC. Due to the excessive runtime of the wave-optics simulation, a parallelized simulation was written to run on a Beowulf supercomputer cluster at the University of California, Los Angeles, using message passing interface. By parallelizing our code to run on a clustered supercomputer, we were able to run larger simulations frequently. An initial observation made during the simulations was that the operational range was inversely proportional to the width of CCR mirrors.

Fig. 7 illustrates simulation results obtained with square mirrors ranging from 31.8 to 57.15 μm wide, simulated with a 1 m^2 photodetector array at an observation distance that is proportional to the mirror size and ranges from 7.5 to 11.25 m. Each

CCR contains ideal mirrors (i.e., radius of curvature $\gg 10$ m) without any mirror misalignment except for the desired mirror misalignment of a single mirror. The angle of mirror misalignment is inversely proportional to the mirror size and simulations are run in the $\langle 111 \rangle$ direction with a 635 nm interrogating optical source.

Fig. 7 illustrates how we can obtain nearly identical results for the interference pattern of a laser reflecting off a CCR and collected on a 1-m^2 photodetector array by simply inversely relating the observation distance with the width of the CCR mirrors provided that the angle of misalignment of the CCR mirrors is also inversely proportional to the width of the CCR mirrors. By continuing this trend, we find that the observation distance of a CCR with 500-μm-wide mirrors is nearly 100 m (98.425 m), assuming incident direction of $\langle 111 \rangle$. However, two non idealities occur when the CCR is rotated off the $\langle 111 \rangle$ axis, the first is that the spot size of the reflected optical beams grows, and the power distribution of the two reflected beams also changes so that the optical signal of one beam grows while the other shrinks. Determining the effect of off-$\langle 111 \rangle$-CCR performance on the detection range is related to the ability of the algorithm to cope with both of these nonidealities.

Fig. 8 illustrates the effect of off-$\langle 111 \rangle$-performance for a CCR with 57.15-μm-wide mirrors at an observation range of 11.25 m, for a CCR with a mirror misalignment of 16.8 mrad, and interrogated in the a) $\langle 111 \rangle$, b) $\langle 223 \rangle$, and c) $\langle 112 \rangle$ directions. CCR reflections were simulated assuming a 1 m^2 photodetector array and a 635 nm optical source.

VIII. Test Setup

For our experiments, the photodetector array was a semitransparent screen and a digital camera. The semitransparent screen was mounted 1 m away from the CCR sensor node. The laser was mounted between the screen and the sensor node so that it was shining orthogonal to the screen and illuminating the CCR. The camera was positioned on the opposite side of the screen so that it would catch the light scattered off of the intermediate screen. Using this technique, we effectively increased the size of the photodetector array while keeping the test setup design simple and inexpensive. However, some of the signal is lost in the semitransparent screen, which reduces the effective operational range. Fig. 9 is an image taken from the photodetector array at a range of 1 m. The large optical beam spot size is due to mirror curvature, nonideal misalignment of fixed mirrors, and the inclusion of etch holes on the mirror surface and can be improved by bulk fabricating flatter mirrors [14].

IX. Measurements

The following experimental results were achieved with a 1 m distance between the zero-power magnetic sensor and the optical diffuser. Each mirror on the CCR is $500 \times 500\ \mu$m^2, with a radius of curvature of 10 cm as measured with a WYKO interferometer. After measuring the mirror curvature and assembling the CCR, the actuation coil was calibrated to obtain a known magnetic field verses the input current. Fig. 10 illustrates the testing results. The deflection of the magnetic element versus magnetic field is greater than the deflection of the mirror for the
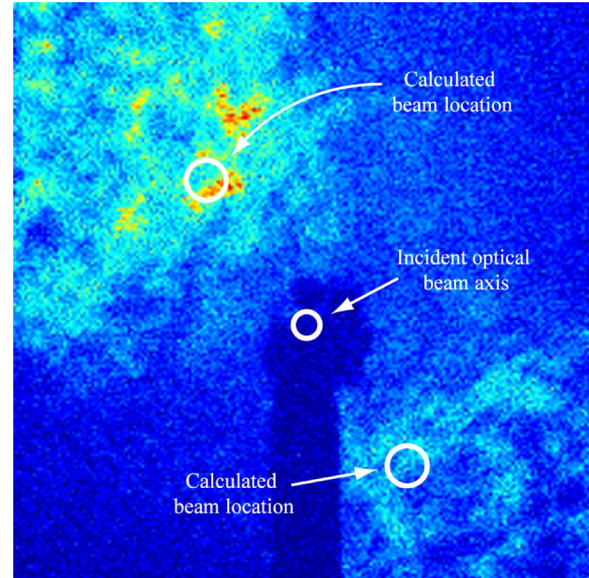

Fig. 9. Image output of photodetector array along with predicted beam locations for a CCR with 500-μm-wide mirrors at a range of 1 m. Beams are wider than those simulated due to mirror curvatures on the order of 10 cm. Flatter mirrors can be fabricated using bulk microfabricated mirrors [17].
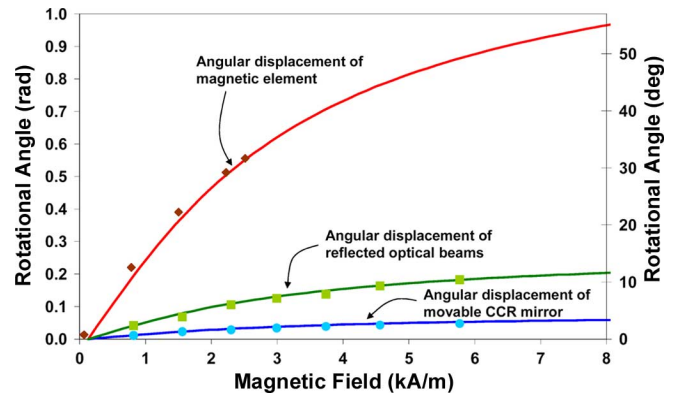

Fig. 10. Angular displacement of the magnetic element, reflected optical beams, and movable CCR mirror as a function of applied magnetic field. Solid line represents theoretical results and points are measured data. The incident direction of the laser is in the $\langle 1, 1, \sqrt{2} \rangle$ direction, causing the reflected optical beams to have a full angle of divergence that is 3.46 times the angle of the mirror misalignment.

same magnetic field because the mirror is coupled to the torsion beam instead of the magnetic element, as discussed earlier. The incident direction of the laser is in the $\langle 1, 1, \sqrt{2} \rangle$ direction, causing the reflected optical beams to have a full angle of divergence equal to 3.46 times the angle of misalignment.

The theoretical detectable field for a sensor with 1-mm-wide mirrors in the $\langle 111 \rangle$ direction, magnetic elements 1 mm long, 100 μm wide, and 10 μm thick, torsion beams that are 4 μm wide, 2 μm thick, and 100 μm long is around 1.6 A/m (2 μT) (using magnetometer deflection curves measured in [4]), and more conservative limits on the detectable field would likely push the detectable field into tens of microtesla. While other magnetometer technologies are capable of detecting fields that are subnanotesla [17], the benefit of this paper is creating a magnetometer that is capable of operating without any power consumption at the remote location.

X. Conclusion

It is possible to create zero-power magnetometers that can be optically interrogated by a remote laser and photodetector array. A micromachined CCR and ferromagnetic MEMS magnetometer have been integrated and used to detect magnetic fields varying from 820 A/m to 6 kA/m with an uncertainty of 90 A/m at a 1 m optical-interrogation range. The use of CCRs in an analog-modulation mode enables simplified sensor-node architectures by eliminating the need for sensing circuitry, power supplies, and radio equipment. The result is a tremendous reduction in size and cost of a sensor node. The first-generation prototype zero-power magnetometers only required a volume of ~ 1.5 mm^3. It is expected that subsequent sensor nodes could be even smaller. Theoretically, analog CCRs have the capability of operating in the 100 m range but are limited by mirror curvature, roughness, etch-hole density, and diffraction. More work can be done to improve sensor performance by reducing mirror curvature, increasing mirror size through bulk-fabricated mirrors [14], and increasing sensor sensitivity by increasing the magnetic volume and attaching the mirrors directly to the magnetic elements. Also more studies can be performed to study the affects of etch holes on the zero-power-sensor sensitivity.

References

[1] D. Kim, I. B. Goldberg, and J. W. Judy, "Micromachined amperometric nitrate sensor with integrated microfluidics," in *Proc. Solid-State Sens. Actuator Microsyst. Workshop*, Hilton Head Island, SC, Jun. 6–10, 2004, pp. 97–98.

[2] J. A. Stankovic, T. E. Abdelzaher, L. Chenyang, S. Lui, and J. C. Hou, "Real-time communication and coordination in embedded sensor networks," *Proc. IEEE*, vol. 91, no. 7, pp. 1002–1022, Jul. 2003.

[3] H. H. Yang, N. V. Myung, J. K. Yee, D.-Y. Park, B.-Y. Yoo, M. Schwartz, K. Nobe, and J. W. Judy, "Ferromagnetic micromechanical magnetometers," in *Proc. 11th Int. Conf. Solid State Sens. Actuators (Transducers '01)*, Munich, Germany, Jun. 10–14, 2001, pp. 164–167.

[4] H. H. Yang, N. V. Myung, J. K. Yee, D.-Y. Park, B.-Y. Yob, M. Schwartz, K. Nobe, and J. W. Judy, "Ferromagnetic micromechanical magnetometer," *Sens. Actuators A, Phys.*, vol. A97–A98, pp. 88–97, Apr. 2002.

[5] J. K. Yee, H. H. Yang, and J. W. Judy, "Dynamic response and shock resistance of ferromagnetic micromechanical magnetometers," in *Proc. 15th IEEE Int. Conf. Micro Electro Mech. Syst.*, Las Vegas, NV, Jan. 20–24, 2002, pp. 308–311.

[6] ——, "Shock resistance of ferromagnetic micromechanical magnetometers," *Sens. Actuators A, Phys.*, vol. A103, no. 1–2, pp. 242–252, Jan. 2003.

[7] D. J. Vasquez and J. W. Judy, "Zero-power magnetometers with remote optical interrogation," in *Proc. 17th IEEE Int. Conf. Micro Electro Mech. Syst.*, Maastricht, The Netherlands, Jan. 25–29, 2004.

[8] M. Tubaishat and S. Madria, "Sensor networks: An overview," *IEEE Potentials*, vol. 22, no. 2, pp. 20–23, Apr. 2003.

[9] B. A. Warneke, M. D. Scott, B. S. Leibowitz, Z. Lixia, C. L. Bellew, J. A. Chediak, J. M. Kahn, B. E. Boser, and K. S. J. Pister, "An autonomous 16 mm/sup 3/solar-powered node for distributed wireless sensor networks," in *Proc. IEEE SENSORS 2002*, Orlando, FL, Jun. 12–14, 2002, pp. 1510–1515.

[10] M. Suster, W. H. Ko, and D. J. Young, "Optically-powered wireless transmitter for high-temperature MEMS sensing and communication," in *Proc. IEEE Int. Solid-State Sens. Actuators Conf.*, Boston, MA, Jun. 8–12, 2003, pp. 1703–1706.

[11] S. Chandra, "Wireless network interface energy consumption," *Multimedia Syst.*, vol. 9, no. 2, pp. 185–201, Aug. 2003.

[12] ——, "Wireless network interface energy consumption implications of popular streaming formats," in *Proc. Multimedia Computing and Networking 2002*, San Jose, CA, Jan. 23–24, 2002, pp. 85–99.

[13] L. Zhou, J. M. Kahn, and K. S. J. Pister, "Corner-cube retroreflectors based on structure-assisted assembly for free-space optical communication," *J. Microelectromech. Syst.*, vol. 12, no. 3, pp. 233–242, Jun. 2003.

[14] L. Zhou, K. S. J. Pister, and J. M. Kahn, "Assembled corner-cube retroreflector quadruplet," in *Proc. 15th IEEE Int. Conf. Micro Electro Mech. Syst.*, Las Vegas, NV, Jan. 20–24, 2002, pp. 556–559.

[15] K. W. Markus, "MEMS infrastructure: The multi-user MEMS process (MUMPs)," *Proc. SPIE*, vol. 2639, pp. 54–63, Oct. 1995.

[16] S. H. Liao, "Electrodeposition of magnetic materials for thin-film heads," *IEEE Trans. Magn.*, vol. 26, no. 1, pp. 328–332, Jan. 1990.

[17] P. Ripka, *Magnetic Sensors and Magnetometers*. Boston, MA: Artech House, 2001.

Daniel J. Vasquez (S'01) received the B.S. and M.S. degrees in electrical engineering from the University of California, Los Angeles, in 2001 and 2004, respectively, where he is currently pursuing the Ph.D. degree.

He was a Communications System Engineer with TRW Space and Electronics (currently Northrop Grumman Corporation) between 2001 and 2002. His research interests include optical and magnetic MEMS devices.

Mr. Vasquez received the Eugene Cota-Robles Fellowship award in 2001.

Jack W. Judy (S'87–M'96–SM'02) received the B.S.E.E. degree *(summa cum laude)* from the University of Minnesota, Minneapolis, in 1989 and the M.S. and Ph.D. degrees from the University of California, Berkeley, in 1994 and 1996, respectively.

In his doctoral research he developed a novel ferromagnetic microactuator technology that is useful for a variety of applications, including optical, RF, and biomedical MEMS. After graduation he was with Silicon Light Machines, Inc., Sunnyvale, CA, an optical-MEMS startup company, from 1996 to 1997. He has been on the Faculty of the Electrical Engineering Department, University of California, Los Angeles (UCLA), since 1997, where he is currently an Associate Professor. At UCLA he is Chair of the MEMS and Nanotechnology major field of the Electrical Engineering Department, Director of the Nanoelectronics Research Facility, and Director of the UCLA NeuroEngineering Training Program, which is an IGERT program supported by the National Science Foundation and sponsored jointly by the Biomedical Engineering Interdepartmental Program and the Brain Research Institute. His present research interests include ferromagnetic MEMS magnetometers, magnetically reconfigurable frequency-selective surfaces, nanomagnetomechanical devices, chemical sensors, and a variety of neuroengineering projects, such as micromachined patch-clamp systems with integrated microfluidics, microprobes for Parkinson's disease research, microactuator-imbedded ventricular catheters for hydrocephalus, inexpensive and robust 3-D cortical microelectrode arrays, electrode arrays for retinal prosthetics, simulating prosthetic vision, wireless neural transceivers for basic neuroscience research, and neural control systems for spinal cord injury, ocular motility, and deep brain stimulation.